JACS
JOURNAL OF THE AMERICAN CHEMICAL SOCIETY
pubs.acs.org/JACS
Article

^{29}Si NMR Spectroscopy as a Probe of s- and f-Block Metal(II)–Silanide Bond Covalency

Benjamin L. L. Réant, Victoria E. J. Berryman, Annabel R. Basford, Lydia E. Nodaraki, Ashley J. Wooles, Floriana Tuna, Nikolas Kaltsoyannis,* David P. Mills,* and Stephen T. Liddle*

Cite This: J. Am. Chem. Soc. 2021, 143, 9813–9824

ABSTRACT: We report the use of ^{29}Si NMR spectroscopy and DFT calculations combined to benchmark the covalency in the chemical bonding of s- and f-block metal–silicon bonds. The complexes $[M(Si^tBu_3)_2(THF)_2(THF)_x]$ (**1-M**: M = Mg, Ca, Yb, x = 0; M = Sm, Eu, x = 1) and $[M(Si^tBu_2Me)_2(THF)_2(THF)_x]$ (**2-M**: M = Mg, x = 0; M = Ca, Sm, Eu, Yb, x = 1) have been synthesized and characterized. DFT calculations and ^{29}Si NMR spectroscopic analyses of **1-M** and **2-M** (M = Mg, Ca, Yb, No, the last *in silico* due to experimental unavailability) together with known $\{Si(SiMe_3)_3\}^-$-, $\{Si(SiMe_2H)_3\}^-$-, and $\{SiPh_3\}^-$-substituted analogues provide 20 representative examples spanning five silanide ligands and four divalent metals, revealing that the metal-bound ^{29}Si NMR isotropic chemical shifts, δ_{Si}, span a wide (~225 ppm) range when the metal is kept constant, and direct, linear correlations are found between δ_{Si} and computed delocalization indices and quantum chemical topology interatomic exchange-correlation energies that are measures of bond covalency. The calculations reveal dominant s- and d-orbital character in the bonding of these silanide complexes, with no significant f-orbital contributions. The δ_{Si} is determined, relatively, by paramagnetic shielding for a given metal when the silanide is varied but by the spin–orbit shielding term when the metal is varied for a given ligand. The calculations suggest a covalency ordering of No(II) > Yb(II) > Ca(II) ≈ Mg(II), challenging the traditional view of late actinide chemical bonding being equivalent to that of the late lanthanides.

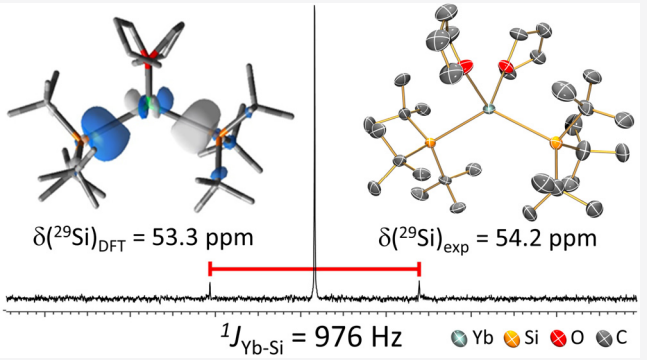

INTRODUCTION

While the qualitative framework of Pauling's conceptual model of chemical bonding from ionic to covalent is in general largely straightforward,[1] the fine detail of covalency in the context of the valence shell is an enduring topic of debate because it is a difficult phenomenon to quantify experimentally and computationally.[2] In order to address this fundamental challenge, it is necessary to appreciate that valence-shell covalency can occur through two different mechanisms: (i) valence orbital overlap driven and (ii) valence orbital energy degeneracy driven.[3] While the former term is most familiar in chemistry and is applicable across most of the periodic table when valence orbitals have sufficient spatial reach to ligand frontier orbitals, the latter concept is often found in physics and emerges as being particularly important for the 5f elements. This is because 5f orbitals can be spatially available for type i bonding or can be energetically, but not spatially, available and thus type ii bonding prevails, most notably as the actinide series is traversed left to right.[2−4]

Three principal methods have emerged to experimentally probe valence shell covalency in metal–ligand linkages, each usually underpinned by quantum chemical investigations. Ligand K-edge X-ray absorption near-edge spectroscopy (XANES) probes the transition intensities of ligand core to valence orbitals that interact with the orbitals of a metal ion;[5] for the f block this technique mainly probes mechanism ii.[6] Electron paramagnetic resonance (EPR) spectroscopy can be used to quantify the spin density of metal-based unpaired electrons at ligand nuclei with nonzero nuclear spin through "superhyperfine" interactions in paramagnetic complexes; thus, it can provide data on metal–ligand bonding,[7] but whether this constitutes mechanism i or ii is an open question and is specific to each case examined. Nuclear magnetic resonance (NMR) spectroscopy provides chemical shift data, which potentially constitutes a direct probe of the electronic environment of a given nucleus, and when this is combined with density functional theory (DFT), it generates a powerful reporter of

Received: March 26, 2021
Published: June 25, 2021

https://doi.org/10.1021/jacs.1c03236
J. Am. Chem. Soc. 2021, 143, 9813–9824

covalency with many ligand nuclei.[8] Where the f block is concerned, solution (^{1}H,[9] ^{13}C,[10] ^{15}N,[11] ^{77}Se,[12,13] and ^{125}Te[13]) and solid-state (^{15}N,[14] ^{17}O,[15] and ^{19}F[16]) studies of ligated nuclei have been reported, but there have not yet been any corresponding studies involving ^{29}Si NMR spectroscopy.

Given that molecular f-block silicon chemistry is developing[17] and that elegant benchmarking studies have been performed for ^{29}Si NMR spectroscopy in the main-group and d transition-metal arenas,[18] it is an opportune time to introduce ^{29}Si NMR studies of covalency to the f block. We recently reported actinide (An)−silanide complexes[19] and sought to extend this work to lanthanide (Ln) derivatives, recognizing that diamagnetic 4f^{14} Yb(II) constitutes an ideal test bed to delineate covalency in f-block M(II)−Si bonds by ^{29}Si NMR spectroscopy, and a range of Ln[17,20] and group 2[21] silanide complexes already exist to enable rigorous and meaningful comparisons to be made.

Here we report the synthesis and characterization of new M(II) (M = Yb, Sm, Eu) bis(trialkylsilanide) complexes utilizing $(Si^tBu_3)^-$ and $(Si^tBu_2Me)^-$ triorganosilanide ligands. To provide a robust family for comparison, we have augmented this work with the corresponding Mg(II) and Ca(II) derivatives. Taken together with existing Ln and group 2 bis(triarylsilanide) ($(SiPh_3)^-$) and bis(trisilylsilanide) ($\{Si(SiR_3)_3\}^-$) derivatives, we have studied these complexes with quantum chemical techniques and also studied hypothetical No(II) congeners, which are experimentally impossible to acquire, *in silico*. We combine ^{29}Si NMR spectroscopy with DFT calculations to study 20 examples spanning five silanide ligands with four divalent metals (Yb, No, Mg, Ca), revealing for the first time direct, linear correlations between the observed isotropic metal-bound ^{29}Si NMR chemical shifts, δ_{Si}, and computed quantum theory of atoms in molecules (QTAIM) delocalization indices (DI(M,Si)) and quantum chemical topology (QCT) interatomic exchange-correlation energies (V_{XC}(M,Si)) that are measures of bond covalency. These investigations reveal a dominance of s- and d-orbital character in the bonding of these silanide complexes, with no appreciable f-orbital contributions, and the δ_{Si} chemical shifts are determined by paramagnetic shielding, σ^{P}, when the metal is constant and the ligand is varied but spin−orbit shielding, σ^{SO}, when the metal is varied for a given ligand. This emphasizes that these M(II)−Si linkages have a polarized-covalent nature and also that their covalency is sensitively reported by ^{29}Si NMR spectroscopy, representing type i covalency. This permits us to order the covalency of these M(II)−Si linkages as No(II) > Yb(II) ≥ Ca(II) ≈ Mg(II). This is particularly significant for No(II) vs Yb(II) because classically the chemical bonding of the late An metals is regarded as being of equivalent covalency to the late Ln metals, not greater than as is often the case for early An metals in comparison to early Ln metals.

RESULTS

Synthetic Considerations. Treatment of $[YbI_2(THF)_2]$[22] with 2 equiv of $NaSi^tBu_3$[23] or $NaSi^tBu_2Me$[24] in THF, followed by workup, affords the Yb(II) bis(trialkylsilanide) complexes $[Yb(Si^tBu_3)_2(THF)_2]$ (**1-Yb**) and $[Yb(Si^tBu_2Me)_2(THF)_3]$ (**2-Yb**) in isolated crystalline yields of 42 and 36%, respectively (Scheme 1). Complex **1-Yb** can also be prepared by the reaction of $YbCl_3$ with 3 equiv of $NaSi^tBu_3$ in THF followed by recrystallization from pentane. However, in addition to salt elimination this reaction requires reduction of Yb(III) to Yb(II) with concomitant formation of $^tBu_3SiSi^tBu_3$ by oxidative coupling, confirmed to occur by ^{29}Si NMR spectroscopy of reaction mixtures[25] and comparison to an authentic sample of $^tBu_3SiSi^tBu_3$,[26] resulting in a low (14%) isolated crystalline yield. In order to support the formulations of **1-Yb** and **2-Yb** and systematically correlate ^{29}Si NMR comparisons, we also prepared $[M(Si^tBu_3)_2(THF)_2(THF)_x]$ (**1-M**: M = Mg, Ca, x = 0; M = Sm, Eu, x = 1) and $[M(Si^tBu_2Me)_2(THF)_2(THF)_x]$ (**2-M**: M = Mg, x = 0; M = Ca, Sm, Eu, x = 1); **1-Mg** has been reported previously.[21d]

Scheme 1. Synthesis of 1-M and 2-M

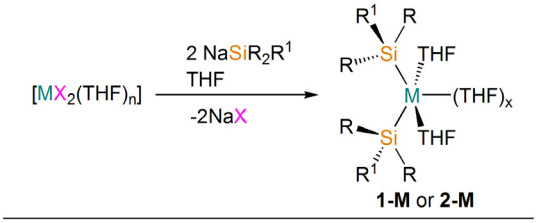

M = Mg; X = Br; n = 0
Ca; X = Br; n = 0
Yb; X = I; n = 2
Sm; X = I; n = 2
Eu; X = I, n = 2

1-M (R = R^1 = ^{t}Bu): Mg; x = 0
Ca; x = 0
Yb; x = 0
Sm; x = 1
Eu; x = 1

2-M (R = ^{t}Bu, R^1 = Me): Mg; x = 0
Ca; x = 1
Yb; x = 1
Sm; x = 1
Eu; x = 1

Complexes **1-M** and **2-M** have been characterized by NMR and ATR-IR spectroscopy and elemental analyses. Complexes **1-Ln** and **2-Ln** have also been characterized by optical spectroscopy, with TD-DFT calculations performed for **1-Yb** and **2-Yb** to assign absorption features and provide experimental validation of the calculations below. Complexes **1-Sm**, **1-Eu**, **2-Sm**, and **2-Eu** were characterized by the Evans magnetic moment method and for Eu EPR spectroscopy (X- and Q-bands).[25]

Solid-State Structures. The solid-state structures of **1-M** and **2-M** were determined by single-crystal X-ray diffraction;[25] **1-Yb** and **2-Yb** are shown in Figure 1. Complex **1-Yb** adopts a pseudotetrahedral geometry with a Si−Yb−Si bond angle (127.19(5)°) that is similar to the Si−Ca−Si angle in the

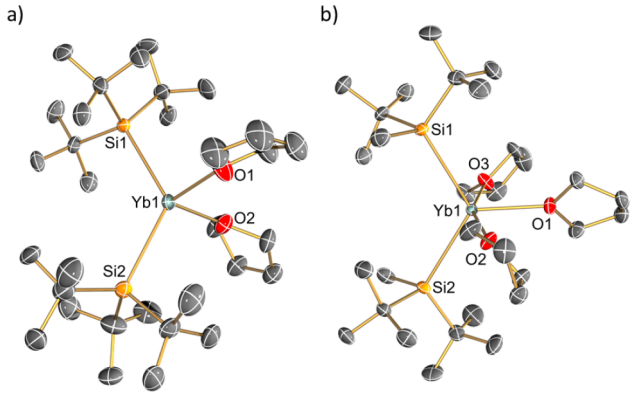

Figure 1. Molecular structures of (a) **1-Yb** and (b) **2-Yb** at 150 K with selective atom labeling. Displacement ellipsoids are set at the 30% probability level, and hydrogen atoms are omitted for clarity.

https://doi.org/10.1021/jacs.1c03236
J. Am. Chem. Soc. 2021, 143, 9813−9824

Table 1. Natural Hybrid Orbital Overlap, Natural Population Analysis Charges, Mean M% and Si% Contributions, and Atomic Orbital Character of the Orbitals (%) from the Precursor Orbitals for the M−Si Bonding Natural Localized Molecular Orbitals in 1-5-M (M = Mg, Ca, Yb, No) Calculated at the PBE0 Functional Level

						M orbital contribution (%)				Si orbital contribution (%)	
	complex	natural hybrid orbital overlap[d]	NPA charge (M/Si)	M[c] (%)	Si[c] (%)	s	p	d	f	3s	3p
1-No	$[No(Si^tBu_3)_2(THF)_2]$[a]	0.585	+1.13/+0.77	11.49	84.58	84.06	0.29	15.36	0.31	39.59	60.18
2-No	$[No(Si^tBu_2Me)_2(THF)_3]$[a]	0.580	+1.14/+0.73	11.37	84.87	80.69	0.32	18.79	0.21	41.80	57.97
3-No	$[No(SiPh_3)_2(THF)_4]$[a]	0.579	+1.31/+0.65	7.40	86.26	74.04	0.06	25.79	0.11	43.61	56.26
4-No	$[No\{Si(SiMe_3)_3\}_2(THF)_3]$[a]	0.511	+1.31/−0.90	8.16	87.00	75.87	1.55	22.36	0.22	34.59	65.34
5-No	$[No\{Si(SiMe_2H)_3\}_2(THF)_3]$[a]	0.521	+1.33/−0.88	8.35	87.65	73.66	1.63	24.48	0.24	38.15	61.79
1-Yb	$[Yb(Si^tBu_3)_2(THF)_2]$[b]	0.541	+1.17/+0.74	9.50	86.63	77.91	0.33	21.38	0.39	40.66	59.12
2-Yb	$[Yb(Si^tBu_2Me)_2(THF)_3]$[b]	0.522	+1.17/+0.71	9.64	86.53	71.59	0.51	27.67	0.25	43.17	56.62
3-Yb	$[Yb(SiPh_3)_2(THF)_4]$[20g]	0.560	+1.28/+0.66	6.80	85.49	64.93	0.23	34.74	0.11	42.65	57.19
4-Yb	$[Yb\{Si(SiMe_3)_3\}_2(THF)_3]$[20d]	0.423	+1.32/−0.92	5.94	88.83	71.27	2.03	26.36	0.34	34.73	65.20
5-Yb	$[Yb\{Si(SiMe_2H)_3\}_2(THF)_3]$[20a]	0.452	+1.35/−0.90	6.64	87.30	45.42	0.87	53.54	0.16	36.93	63.01
1-Ca	$[Ca(Si^tBu_3)_2(THF)_2]$[b]	0.487	+1.64/+0.68	6.87	88.96	78.22	0.46	21.33	-	37.96	61.82
2-Ca	$[Ca(Si^tBu_2Me)_2(THF)_3]$[b]	0.481	+1.64/+0.65	6.55	89.89	78.65	0.56	20.80	-	45.84	54.00
3-Ca	$[Ca(SiPh_3)_2(THF)_4]$[21b]	0.446	+1.73/+0.61	4.22	88.63	77.36	0.47	22.18	-	43.74	56.14
4-Ca	$[Ca\{Si(SiMe_3)_3\}_2(THF)_3]$[21c]	0.418	+1.74/−1.00	4.02	90.86	70.57	1.66	27.78	-	36.67	63.27
5-Ca	$[Ca\{Si(SiMe_2H)_3\}_2(THF)_3]$[20a]	0.419	+1.72/−0.95	4.53	91.39	72.85	1.62	25.53	-	41.48	58.48
1-Mg	$[Mg(Si^tBu_3)_2(THF)_2]$[21d]	0.531	+1.47/+0.74	11.27	84.66	98.08	1.64	0.23	-	42.64	57.01
2-Mg	$[Mg(Si^tBu_2Me)_2(THF)_2]$[b]	0.536	+1.44/+0.72	12.19	84.09	97.97	1.78	0.22	-	43.66	55.90
3-Mg	$[Mg(SiPh_3)_2(THF)_2]$[21a]	0.645	+1.45/+0.67	11.88	81.94	97.85	2.29	0.34	-	40.77	58.77
4-Mg	$[Mg\{Si(SiMe_3)_3\}_2(THF)_2]$[21e]	0.510	+1.55/−0.98	9.31	85.64	97.51	1.99	0.48	-	25.35	74.36
5-Mg	$[Mg\{Si(SiMe_2H)_3\}_2(THF)_2]$[20a]	0.496	+1.59/−0.96	9.30	87.14	97.84	2.13	0.03	-	31.68	68.05

[a]This work; characterized *in silico*, but experimentally unavailable. [b]This work; *in silico* and experimentally characterized. [c]Other minor, delocalized contributions, totaling <8% in all cases, to these NLMOs are not included. [d]NHO overlap values of 1 and 0 equate to complete and no orbital overlap of the orbitals on the fragments used in the NBO process of generating NLMOs, respectively.[65]

isostructural **1-Ca** (129.19(2)°) but that is expectedly wider than the Si−Ln−Si angles found in the five coordinate **1-Sm** (118.59(6)°) and **1-Eu** (118.70(7)°). Complex **2-Yb** is also five-coordinate (Si−Yb−Si = 120.19(3)°), with a geometry between trigonal bipyramidal (tbp) and square pyramidal (sp) (τ_5 = 0.62), where the tbp "axial" sites are occupied by THF, and this is similar to the cases of **1-Sm** (τ_5 = 0.49), **1-Eu** (τ_5 = 0.44), **2-Sm** (τ_5 = 0.55), and **2-Eu** (τ_5 = 0.54). The variation in the number of coordinated THF molecules in **1-Ln** and **2-Ln** can be related to a combination of the varying steric demands of the two silanide ligands and also the ionic radii of Yb(II) (1.14 Å), Sm(II) (1.27 Å), and Eu(II) (1.25 Å).[27] In **1-Yb** the Yb−Si bond lengths (average 3.060(3) Å) are indistinguishable by the 3σ criterion from those in **2-Yb** (mean 3.0678(14) Å); as expected, these metrics are very similar to those of the isostructural **1-Ca** and **2-Ca** (3.0678(14) and 3.056(5) Å, respectively), given the similar ionic radii of Yb(II) and Ca(II) (1.12 Å) but shorter than the corresponding Sm−Si and Eu−Si bond lengths (**1-Sm**, 3.261(3) Å; **1-Eu**, 3.258(4) Å; **2-Sm**, 3.2196(10) ang; **2-Eu**, 3.2075(9) Å). On comparison of **1-Ln** and **2-Ln** to $[M\{Si(SiMe_3)_3\}_2(THF)_3]$ (M = Yb, Sm, Eu),[17a,20d] the Ln−Si distances in the latter are slightly shorter than those of **1-Ln** and **2-Ln** for Sm and Eu but are indistinguishable for Yb.

Stability Considerations and NMR Characterization. Crystalline samples of **1-M** and **2-M** can be stored for months at room temperature under dry argon with no signs of decomposition. In contrast, C_6D_6 solutions of **1-Yb** and **2-Yb** decompose at room temperature, as evidenced by the visual darkening of solutions. Monitoring a C_6D_6 solution of **2-Yb** by ^{29}Si NMR spectroscopy revealed complete decomposition to one unidentified species (δ 4.06 ppm) within ∼35 h ($t_{1/2}$ = 2.86 h). However, by using 9/1 C_6D_6/C_4D_8O solutions of **1-Yb** and **2-Yb** the ^{29}Si NMR spectra confirm that the decomposition of **2-Yb** is suppressed to <5% at 7 h and **1-Yb** does not decompose at all. Complexes **1-Mg**, **1-Ca**, **2-Mg**, and **2-Ca** were found to be indefinitely stable in neat C_6D_6. With the stability of these complexes in solution confirmed, we examined their NMR spectra in detail.

The ^{29}Si NMR spectra of **1-Yb** and **2-Yb** exhibit δ_{Si} resonances at 54.19 and 29.24 ppm,[25] each with satellites from $^1J_{Yb-Si}$ coupling of 976 Hz (**1-Yb**) and 921 Hz (**2-Yb**), respectively, assigned as the metal-bound Si centers (^{171}Yb: I = 1/2, 14.3%). The $^1J_{Yb-Si}$ coupling constants for **1-Yb** and **2-Yb** are the largest to date: $[Yb(Cp^*)\{Si(SiMe_3)_3\}(THF)_2]$ (829 Hz);[20f] $[Yb\{Si(SiMe_3)_3\}_2(THF)_3]$ (732 Hz);[20d] $[Yb\{Si(SiMe_3)_3\}\{\mu\text{-}N(SiMe_3)_2\}_2K]$ (716 Hz);[20e] $[Yb\{Si(SiMe_3)_2SiMe_2\}_2(DME)_{1.5}]$ (656 Hz);[20d] $[Yb\{Si(SiMe_3)_2SiMe_2\}_2(THF)_4]$ (633 Hz);[20b] $[Yb\{(Si\{SiMe_3\}_2SiMe_2)_2O\}(THF)_3]$ (633 Hz).[20b] The ^{171}Yb NMR spectra of **1-Yb** and **2-Yb** exhibit resonances at 1044.64 and 825.07 ppm, respectively, with $^1J_{Yb-Si}$ satellites (^{29}Si: I = 1/2, 4.67%), and these can be compared[28] to $[Yb(Cp^*)\{Si(SiMe_3)_3\}(THF)_2]$ (δ_{Yb} 421 ppm)[20f] and $[Yb\{Si(SiMe_3)_3\}\{\mu\text{-}N(SiMe_3)_2\}_2K]$ (δ_{Yb} 1057 ppm).[20e]

https://doi.org/10.1021/jacs.1c03236
J. Am. Chem. Soc. 2021, 143, 9813−9824

Computational Electronic Structure Analysis. To investigate the nature of the Yb−Si bonding in **1-Yb** and **2-Yb**, scalar relativistic, dispersion-corrected, hybrid DFT calculations were performed, including natural localized molecular orbital (NLMO) and QTAIM analyses (Table 1). These results were benchmarked by calculations on **1-Ln** and **2-Ln** for the Sm(II) and Eu(II) analogues; Figure 2 depicts the

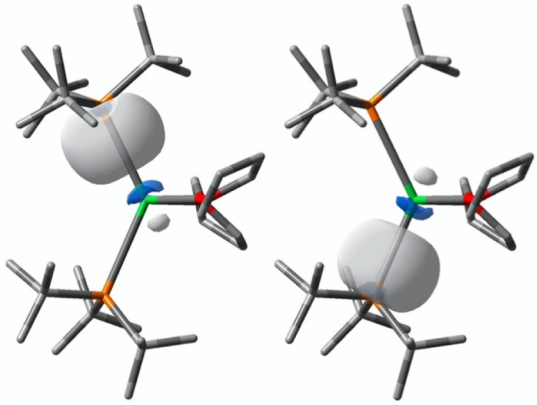

Figure 2. Natural localized molecular orbitals for the Yb−Si bonding interactions in **1-Yb**. The isodensity value is set to 0.05 au, and hydrogen atoms are omitted for clarity.

Yb−Si NLMOs for **1-Yb**, and details of the other complexes can be found in the Supporting Information.[25] We have extended this analysis by performing NLMO and QTAIM calculations on a mixture of experimentally realized (M = Mg(II), Ca(II), Yb(II)) and experimentally inaccessible but predicted (M = No(II)) complexes for five structurally analogous families: $[M(Si^tBu_3)_2(THF)_2]$ (**1-M**, M = Mg, Ca, Yb, No), $[M(Si^tBu_2Me)_2(THF)_2(THF)_x]$ (**2-M**: M = Mg, x = 0; M = Ca, Yb, No, x = 1), $[M(SiPh_3)_2(THF)_y]$ (**3-M**: M = Mg, y = 2; M = Ca, Yb, No, y = 4), $[M\{Si(SiMe_3)_3\}_2(THF)_y]$ (**4-M**: M = Mg, y = 2; M = Ca, Yb, No, y = 3), and $[M\{Si(SiMe_2H)_3\}_2(THF)_y]$ (**5-M**: M = Mg, y = 2; M = Ca, Yb, No, y = 3) (Table 1).[20a,b,d,g,21] Computed M−Si bond lengths[25] are in good agreement with available experimental solid-state data, giving confidence in the computed models.

The computed natural population analysis (NPA) charges for the metals vary by ∼0.6 over the entire series of **1-M**−**5-M**, reflecting varied donation of electron density from the silanide ligands to M centers. Notably, the NPA charges for the alkyl-substituted **1-M** and **2-M** are almost always, like for like, smaller than those of the $(SiPh_3)^-$ and $\{Si(SiR_3)_3\}^-$ **3-M**−**5-M** complexes, suggesting greater covalency in the M−Si linkages of the former pair to the latter grouping. This trend is broadly reproduced in the calculated natural hybrid orbital (NHO) overlaps, which report on the spatial overlap of the hybridized orbitals of M and Si used to construct the NLMOs, but the varied coordination numbers of the M(II) ions due to differing THF coordinations complicates this analysis. The M−Si bonds are dominated by Si contributions (∼81−88%), consistent with their polarized-covalent natures, but for each metal larger M(II) contributions are often found for **1-M** and **2-M** in comparison to **3-M**−**5-M**, which is consistent with the NPA charges and NHO metrics. The composition of the M(II) contributions to the M−Si bonds varies but is always dominated by s character. For Mg(II) the s contributions are >97%, whereas for Ca(II) the s character remains dominant (∼70−78%) while significant (∼20−28%) d contributions emerge. The orbital contribution picture for Ca(II) is largely replicated for Yb(II), with notably negligible (<0.4%) 4f contributions to the bonding consistent with the "core-like" nature of the 4f orbitals, especially at the end of the 4f series. Likewise, though 5f orbitals engage in bonding for the early An metals, by the end of the 5f series, where No(II) is located, they are traditionally considered to also be "core-like", which is reflected in insignificant (<0.4%) 5f contributions and bonding that is dominated by s (∼74−84%) supplemented with d (∼15−26%) contributions. As expected, the Si contributions are composed of s (∼25−46%) and p (∼54−75%) combinations. Finally, we note that, using the M(II)% contribution to these M−Si bonds as a crude proxy of covalency, the covalency of the M−Si bonds analyzed here can be ordered as No(II) ≈ Mg(II) > Yb(II) > Ca(II), but the differences are modest.

Computational Chemical Shift−Covalency Correlation Analysis. We calculated the δ_{Si} chemical shifts of the metal-bound Si-centers for **1-M**−**5-M** using the PBE0 and SAOP functionals; the former, which is a hybrid density functional incorporating 25% of the exact exchange energy from Hartree−Fock theory,[29] has frequently been used to calculate NMR chemical shifts,[9−13] while the latter is less computationally demanding but is also a functional that provides good correlation.[30] We find that both functionals provide computed chemical shifts in good agreement with the experimental data. Plots of calculated δ_{Si} chemical shifts for **1-M**−**5-M** using either PBE0 or SAOP functionals vs experimentally determined δ_{Si} values show excellent agreement at both levels of theory, with mean absolute deviations of 14.5 and 3.6 ppm for PBE0 and SAOP functionals, respectively (Figure 3).

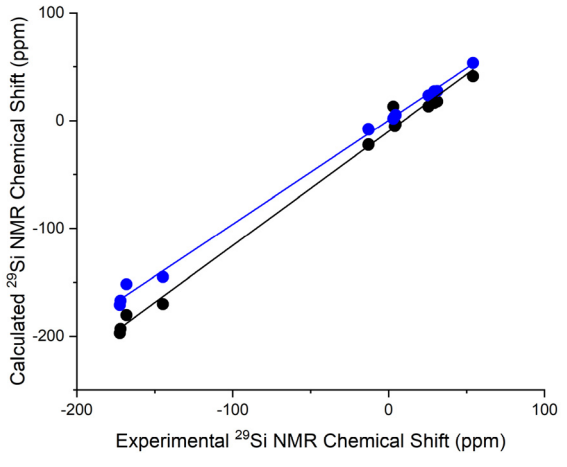

Figure 3. Calculated vs experimentally determined ^{29}Si NMR chemical shifts (where available) for **1-M**−**5-M** at both SAOP (blue circles) and PBE0 (black circles) levels of theory. Linear regression analysis: SAOP, $\delta(^{29}Si)_{calcd} = 0.97 \times \delta(^{29}Si)_{exp} + 0.32$, $R^2 = 0.998$; PBE0, $\delta(^{29}Si)_{calcd} = 1.06 \times \delta(^{29}Si)_{exp} - 10.1$, $R^2 = 0.994$.

Salient experimental and computed properties related to the ^{29}Si NMR chemical shift data for **1-M**−**5-M** are shown in Table 2. As expected, there are small differences (<10 ppm) in the computed diamagnetic σ^d shielding values, since this concerns core electrons. Interestingly, the σ^p shielding values vary little (<10 ppm) within each class of complex when the central metal is varied. However, significant (180−220 ppm)

https://doi.org/10.1021/jacs.1c03236
J. Am. Chem. Soc. 2021, 143, 9813−9824

Table 2. Experimental and Calculated (Using PBE0 and SAOP Functionals) ^{29}Si NMR Chemical Shifts (δ_{Si} in ppm vs $SiMe_4$), Isotropic Shielding Contributions (σ^d = Diamagnetic, σ^p = Paramagnetic, and σ^{SO} = Spin−Orbit Coupling) to the Calculated ^{29}Si NMR Chemical Shift and QCT Bonding Metrics (DI and V_{XC}) for M−Si Bonding Interactions of 1-M−5-M (M = Mg, Ca, Yb, No)[20a,d,g,21]

		δ_{Si}(calcd) (ppm)		σ^d (ppm)		σ^p (ppm)		σ^{SO} (ppm)			
complex	δ_{Si}(exptl) (ppm)	PBE0	SAOP	PBE0	SAOP	PBE0	SAOP	PBE0	SAOP	DI(M,Si)	V_{XC} (M,Si) (au)
1-No	*a*	94.4	102.4	873.9	858.7	−536.6	−494.2	−68.7	−66.5	0.434	−0.0755
2-No	*a*	66.1	77.4	874.0	859.0	−513.1	−472.4	−64.6	−63.6	0.422	−0.0724
3-No	*a*	28.4	35.4	873.3	881.8	−499.8	−486.0	−38.9	−30.8	0.309	−0.0543
4-No	*a*	−119.4	−48.5	879.4	872.4	−338.8	−323.3	−58.2	−53.7	0.409	−0.0675
5-No	*a*	−129.2	−101.0	880.8	875.2	−324.4	−313.9	−64.0	−59.9	0.410	−0.0694
1-Yb	54.2	41.1	53.3	874.0	853.8	−533.6	−489.0	−17.5	−17.8	0.384	−0.0684
2-Yb	29.2	16.4	27.3	873.9	851.7	−511.3	−463.3	−15.3	−15.3	0.357	−0.0637
3-Yb	4.0	−5.3	4.0	874.5	885.0	−498.8	−484.7	−6.7	−3.1	0.276	−0.0499
4-Yb	−144.8	−170.4	−145.2	880.6	869.1	−333.3	−311.9	−13.3	−11.6	0.357	−0.0607
5-Yb	−168.1	−180.3	−151.8	882.2	871.7	−323.8	−306.8	−14.5	−12.7	0.352	−0.0607
1-Ca	25.6	13.0	23.3	875.6	860.9	−533.3	−491.3	8.5	8.2	0.290	−0.0517
2-Ca	3.1	13.0	1.9	874.5	859.5	−510.4	−468.5	8.7	8.3	0.264	−0.0468
3-Ca	−13.0	−22.7	−7.5	874.7	881.4	−497.3	−481.8	9.0	9.1	0.192	−0.0341
4-Ca	−172.3	−197.1	−171.0	880.8	870.8	−329.6	−307.9	9.5	9.3	0.256	−0.0434
5-Ca	−194.6	−208.1	−178.5	881.8	873.8	−319.5	−303.4	9.5	9.3	0.256	−0.0442
1-Mg	31.2	17.7	27.5	874.6	855.9	−538.5	−491.4	9.9	9.2	0.256	−0.0486
2-Mg	4.5	−3.3	5.2	875.2	855.5	−518.0	−468.8	9.9	9.2	0.255	−0.0497
3-Mg	−12.8	−22.0	−8.4	875.0	881.4	−498.9	−481.5	9.6	9.6	0.232	−0.0465
4-Mg	−171.9	−193.1	−167.2	880.5	869.0	−334.5	−310.7	10.7	10.2	0.247	−0.0463
5-Mg	−182.3	−200.8	−179.1	878.9	879.8	−325.4	−316.1	10.7	10.5	0.250	−0.0476

[a]Predicted complex; solution data not available.

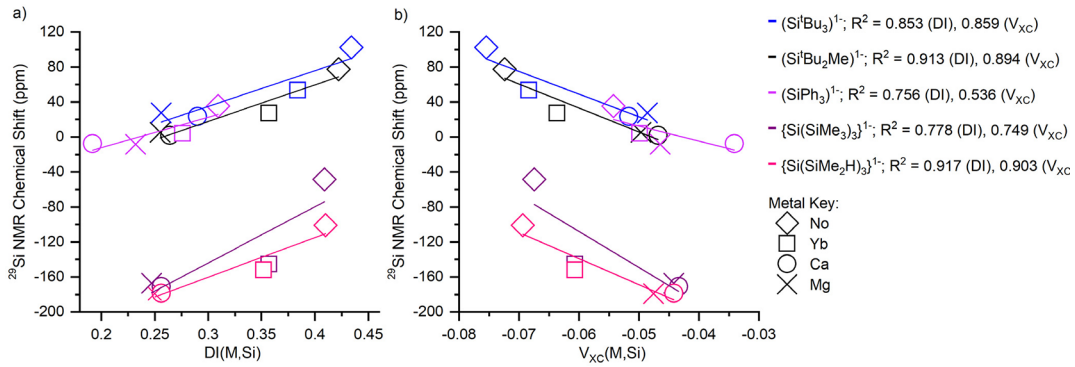

Figure 4. Plots of SAOP-calculated δ_{Si} chemical shifts for **1-M−5-M** vs computed measures of bond covalency: (a) δ_{Si} vs the delocalization index, DI(M,Si); (b) δ_{Si} vs V_{XC}(M,Si).

differences in σ^p values are found upon variation of the silanide ligands but with the metal kept constant, showing that $(SiR_3)^-$ substituents significantly increase the σ^p contributions to the overall δ_{Si} in comparison to $\{Si(SiR_3)_3\}^-$ substituents. Likewise, the σ^{SO} shielding value remains fairly constant for a given metal irrespective of the silanide ligand, but greater variation emerges when the ligand is kept constant and the metal is varied. The most significant σ^{SO} contributions are found for No(II), followed by Yb(II), and then Mg(II) and Ca(II) that are similar to each other; however, it should be noted that the sign of the σ^{SO} is negative for No(II) and Yb(II) but positive for Mg(II) and Ca(II). The large variations in σ^p thus essentially account for the majority of the differences observed in the experimental/calculated δ_{Si} values between electron-donating and electron-withdrawing silanide complexes for a given metal, but conversely when the ligand is constant, it is the σ^{SO} which varies with the metal that produces the variation in δ_{Si}.

The computed DI(M,Si), and QCT V_{XC}(M,Si) values for **1-M−5-M** are given in Table 2. DI is a frequently reported covalency metric and is a QTAIM measure of bond order, whereas V_{XC} defines the contribution to the interaction energy between two atoms to assess covalency.[31] Interestingly, there are only modest variations in these metrics, likely reflecting the polarized nature of these M−Si bonds, but the DI(M,Si) and V_{XC}(M,Si) data can overall be ordered No(II) > Yb(II) > Ca(II) ≈ Mg(II). While this appears contradictory to the MO M% ordering, it is marginal given the small differences in DI for Mg vs Ca. We note that, while the NLMO compositional analysis focuses on covalency within a single orbital, DI is

https://doi.org/10.1021/jacs.1c03236
J. Am. Chem. Soc. 2021, 143, 9813−9824

evaluated over the entirety of the M and Si QTAIM atomic basins and so may return slightly different conclusions. Importantly, when the silanide ligand is kept constant, plotting ^{29}Si chemical shifts using the SAOP functional vs DI(M,Si) or V_{XC}(M,Si) (Figure 4) produces linear correlations and in both cases two ligand groupings emerge with the $(SiR_3)^-$ ligands clustered at more positive δ_{Si} values in comparison to the $\{Si(SiR_3)_3\}^-$ ligands. Similar fits are obtained from the PBE0 data, and those along with individual plots of metal variation per ligand can be found in the Supporting Information.[25]

DISCUSSION

Salt elimination reactions facilitate straightforward access to silanide derivatives of Mg(II), Ca(II), Yb(II), Sm(II), and Eu(II) from divalent halide precursors. Notably, Yb(III) can also afford entry to the Yb(II) derivatives, but this route is inferior to starting with Yb(II), as the Yb(III) to Yb(II) reduction route clearly opens up decomposition pathways. It is interesting to note that the tris(THF) adducts of **1-Ln** and **2-Ln** are unstable in aromatic solution, but addition of THF stabilizes them. This suggests that one, or more, of the coordinated THF molecules can dissociate in solution, opening up one or more vacant coordination sites that facilitate decomposition, but excess donor solvent suppresses this, closing off the decomposition pathway.

The remarkably downfield, that is high-frequency-shifted, ^{29}Si NMR chemical shifts of 54.2 and 29.2 ppm for the metal-bound Si centers for **1-Yb** and **2-Yb** are notable because they are the most positive, deshielded δ_{Si} values for any Yb(II)−Si complex to date.[17a,20] This is because prior examples of Yb−Si complexes have utilized electron-withdrawing silyl and aryl substituents that result in close to zero or negative δ_{si} chemical shifts. Nevertheless, the observation that the δ_{Si} value shifts ∼200 ppm by replacing $\{Si(SiMe_2H)_3\}^-$ with $(Si^tBu_3)^-$ in otherwise identical $[Yb(SiR_3)_2(THF)_3]$ complexes is notable and shows how sensitive a reporter ^{29}Si NMR spectroscopy is to changes in the electronic structure of silanides, and similar levels of sensitivity are found for Mg(II) and Ca(II) congeners. Even minor changes within a class, i.e. replacing $(Si^tBu_3)^-$ in **1-Yb** with $(Si^tBu_2Me)^-$ in **2-Yb**, results in a δ_{Si} shift of 25 ppm, the majority of which is due to the σ^p component with only a minor σ^{SO} component; this is regarded as significant because although NLMO data in Table 1 reveal variance in the percent s character, the range of variance (<7%) is small. Though the potential effect of an additional THF ligand in **2-Yb** in comparison to **1-Yb** cannot be disregarded, it is likely minor (cf. the essentially identical Yb−Si distances in **1-Yb** and **2-Yb**). The large downfield ^{171}Yb chemical shifts of **1-Yb** and **2-Yb** likely reflect significantly deshielded Yb(II) ions, but a rigorous analysis of this aspect will require further examples of ^{171}Yb NMR chemical shift data to enable correlations to be established.

Our calculations, which reproduce experimental δ_{Si} values satisfactorily, consistently find that for a given metal that there is little variation in the σ^d and, as a proportion, the σ^{SO} shielding contributions to the δ_{Si} values for **1-M−5-M**. The observed ^{29}Si chemical shifts thus, for a given metal, largely depend on variations of the σ^p values. Ramsey's general theory of magnetic shielding rationalizes σ^{iso} by primarily partitioning shielding contributions into σ^d and σ^p, which are dependent on electron orbital angular momenta. Although this many-electron state description does not directly relate to DFT MOs and their energies, especially those derived from hybrid functionals, it provides an approximate framework in which to rationalize NMR shielding values. According to Ramsey's formula,[32] σ^p is proportional to (i) the extent of mixing between magnetically coupled orbitals induced by a magnetic field, (ii) $1/r^3$ of the shielding electrons where r is the radial expansion, and (iii) $1/\Delta E$, where ΔE is the energy gap between the corresponding occupied and unoccupied orbitals. The first two relate to bond covalency and atomic charges, and also because as a bonded atom withdraws electron density from the NMR nucleus, this will contract the valence orbitals, reducing r and thus increasing the magnitude of $1/r^3$ and σ^p (i.e., the NMR nuclei are more deshielded). These relationships therefore link covalency directly to σ^p,[13] and they should be correlated directly for a given series of complexes, when the ΔE term is fairly invariant (Table S9), clearly indicating that the covalency being described is orbital overlap driven in nature.

For a given metal, the δ_{Si} values for **1-M−5-M** are largely determined by σ^p, and from Ramsey's formula σ^p is proportional to covalency. Since δ_{Si} is an experimentally measurable quantity, it follows that δ_{Si} is a good reflection of computed bond covalency metrics if a linear relationship can be established. Indeed, this is the case for DI(M,Si) and V_{XC}(M,Si) (Figure 4). That two ligand groupings emerge with the $(SiR_3)^-$ ligands clustered at more positive δ_{Si} values in comparison to the $\{Si(SiR_3)_3\}^-$ ligands is interesting, as this reflects the former engaging in slightly more covalent M−Si bonding interactions in comparison to the latter for a given metal. It is also important to note that the two silanide ligand groupings are offset linearly from one another on the δ_{Si} scale and not in an exponential manner; such exponential correlations occur when additional and large σ^{SO} effects from 5f-orbital contributions are included in the final δ value, as has been found to be the case for Th and U chalcogenido complexes.[13] This is consistent with the NLMO descriptions of **1-M−5-M**, which exhibit little, if any, 5f character, and so the σ^{SO} contributions are restricted to those originating from d-orbital character, being computed to be up to 69 ppm for No(II), which is much smaller than the σ^{SO} shielding values typically found for Th and U due to 5f-orbital bonding contributions (∼100−400 ppm).[9−13]

As stated above, σ^{SO} changes little for a given metal for **1-M−5-M**. However, when the ligand is kept constant and the metal is varied, significant changes in σ^{SO} are observed. For example, for **1-M** σ^{SO} varies from 8.5 ppm for **1-Ca** to −68.7 ppm for **1-No**. These changes arise from variations in heavy-atom effects on heavy-atom shielding (HAHA).[8] For **1-Mg** and **1-Ca**, the HAHA stems from Si's relativistic effects on its own shielding, i.e. it is largely atomic in nature; it is noticeable that the value of σ^{SO} for Si in $SiMe_4$, 10.5 ppm, is very similar to that in **1-Mg** and **1-Ca**. In contrast, for **1-Yb** and **1-No** we see the effect of the heavy metal on the Si shielding, transmitted via covalent bonding. To probe this in more detail, we have analyzed the shielding in **1-M** at the PBE0 level, using the NLMO-based method implemented in the ADF code, since the NLMO composition data this process produces can be checked against our Gaussian data (Table 1). The five most significant contributors to the $\sigma^p + \sigma^{SO}$ term (ADF reports the sum of these two terms in the NLMO shielding analysis) are the three Si−C bonding NLMOs, a Si p core orbital, and the M−Si bonding NLMO (the orbitals shown in Figure 2 for **1-Yb**). The contribution of the latter to the $\sigma^p + \sigma^{SO}$ term varies as −75.7, −70.6, −128.8, and −202.8 ppm from **1-Mg** to **1-**

https://doi.org/10.1021/jacs.1c03236
J. Am. Chem. Soc. 2021, 143, 9813−9824

No. As the σ^{P} component is essentially constant across this family, the changes stem from the σ^{SO} term, and the M−Si bonding NLMO contributions to $\sigma^{P} + \sigma^{SO}$ are correlated with the overall value of $\sigma^{P} + \sigma^{SO}$ with $R^2 = 0.985$. The changes in $\sigma^{P} + \sigma^{SO}$ for the other principal NLMO contributors are generally much smaller than those of the M−Si bonding NLMO and do not correlate with the overall change in $\sigma^{P} + \sigma^{SO}$. The composition of the M−Si bonding NLMOs returned by ADF are similar to those reported from our Gaussian calculations in Table 1. These orbitals have significant Si 3s character and, for **1-Ca**, **1-Yb**, and **1-No**, small contributions from metal d orbitals. PBE0 calculations of the splitting of the 3d, 5d, and 6d orbitals of atomic Ca, Yb, and No yield 0.014, 0.094, and 0.161 eV, respectively. Hence the composition of the M−Si bonding NLMO is such that it is well set up to transmit metal d-based spin−orbit shielding to the Si via Si 3s character, due to the Fermi contact mechanism enabling induced spin polarization to be transferred to the NMR nucleus in question.[33] Thus, we conclude that the contributions of this orbital are the primary driver of the changes seen in σ^{SO} in Table 2.

We note that the calculations produce a consistent picture, in which the complexes with the most positive δ_{Si} values typically also have M(II)−Si linkages that exhibit (i) the largest M(II)-orbital %, (ii) the largest DI(M,Si) and V_{XC}(M,Si) values, (iii) M(II) ions with the lowest NPA charges, and (iv) the largest $^{1}J_{Yb-Si}$ coupling constants (where experimental data are available). Thus, an internally consistent bonding picture and quantification of the levels of covalency in these M−Si bonds emerges, where complexes with the most positive δ_{Si} values are the most covalent. This reveals a covalency ordering of No(II) > Yb(II) > Ca(II) ≈ Mg(II), of significance because the bonding of late An metals is often regarded to be the same as that of late Ln metals.

CONCLUSIONS

To conclude, we have reported the synthesis and characterization of new divalent Yb, Sm, Eu, Mg, and Ca complexes supported by triorganosilanide ligands. In combination with previously reported triaryl- and trisilylsilanide congeners a robust family of complexes for comparison is established. We have studied the Yb, Ca, and Mg complexes with quantum chemical techniques and also examined hypothetical, and experimentally inaccessible, No(II) derivatives. By combining ^{29}Si NMR spectroscopy and DFT calculations, we have thus studied 20 related complexes, revealing for the first time direct, linear correlations between the observed δ_{Si} and DI(M,Si) and V_{XC}(M,Si) metrics, which are measures of bond covalency. The calculations reveal a dominance of s- and d-orbital character in the M−Si bonding of these silanide complexes, with no appreciable f-orbital contributions. For a given metal, the variation in δ_{Si} with the ligand is determined by the σ^{P} shielding term, whereas for a given ligand, variation in δ_{Si} with the metal is a function of σ^{SO}. This emphasizes that the covalency in these polarized-covalent M(II)−Si linkages is sensitively reported by ^{29}Si NMR spectroscopy and is overlap-driven. The calculations, and δ_{Si} chemical shift data where available, suggest a covalency ordering of these M(II)−Si linkages as No(II) > Yb(II) > Ca(II) ≈ Mg(II). This challenges the classical picture of the chemical bonding of the late An metals being regarded as of equivalent covalency to, and not greater than, that of the late Ln metals, as is often the case for early An metals in comparison to early Ln metals.

EXPERIMENTAL SECTION

General Methods and Materials. All manipulations were conducted under argon with the strict exclusion of oxygen and water by using Schlenk line and glovebox techniques. THF was purged with ultrahigh-purity-grade argon (Airgas) and passed through columns containing alumina catalyst and molecular sieves before use. Hexane was dried by refluxing over potassium and was stored over a potassium mirror and then degassed before use. For NMR spectroscopy, C_6D_6 and C_4D_8O were dried by refluxing over K and were vacuum-transferred and degassed by three freeze−pump−thaw cycles before use.

NMR spectra (see Table S1 for experimental parameters and Figures S1−S30) were recorded on either a Bruker AVIII HD 500 spectrometer operating at 500.19 (^{1}H), 125.77 (^{13}C), or 87.52 (^{171}Yb) MHz or a Bruker AVIII HD 400 spectrometer operating at 400.07 (^{1}H) or 79.48 (^{29}Si) MHz. NMR spectra were referenced to TMS (^{1}H, ^{13}C, ^{29}Si) or the proton frequency of the solvent used (^{171}Yb). ATR-IR spectra were recorded as microcrystalline powders using a Bruker Alpha spectrometer with a Platinum-ATR module (see Figures S31−S41). UV−vis−NIR spectroscopy (see Table S2 for TD-TDFT modeling and Figures S42−S48) was performed on samples in Young tap-appended 10 mm path length quartz cuvettes on an Agilent Technologies Cary Series UV−vis−NIR spectrophotometer from 175 to 3300 nm. X-band (~9.4 GHz) and K-band (~23.9 GHz) EPR data on **1-Eu** and **2-Eu** (Figures S49 and S50) were recorded on a Bruker E580 spectrometer. Crystals of **2-Mg**, **2-Ca**, **2-Sm**, **2-Eu**, and [{NaSi^{t}Bu$_2$Me}$_4$] were examined using an Agilent Supernova diffractometer, equipped with an Eos CCD area detector and a microfocus source with Mo Kα radiation (λ = 0.71073 Å). Crystals of **1-Sm**, **1-Eu**, **1-Yb**, and **2-Yb·C$_5$H$_{12}$** were examined using a Rigaku Xcalibur2 diffractometer, equipped with an Atlas CCD area detector and a sealed-tube source with graphite-monochromated Mo Kα radiation (λ = 0.71073 Å). Crystals of **1-Ca** and [Na(μ-Si^{t}Bu$_2$Me)]$_\infty$ were examined using a Rigaku FR-X diffractometer, equipped with a HyPix 6000HE photon-counting pixel array detector with mirror-monochromated Mo Kα (λ = 0.71073 Å) or Cu Kα (λ = 1.5418 Å) radiation. Intensities were integrated from data recorded on 0.5° ([Na(μ-Si^{t}Bu$_2$Me)]$_\infty$) or 1° (**1-Ca**, **1-Sm**, **1-Eu**, **1-Yb**, **2-Mg**, **2-Ca**, **2-Sm**, **2-Eu**, **2-Yb·C$_5$H$_{12}$**, [{NaSi^{t}Bu$_2$Me}$_4$]) frames by ω rotation. Cell parameters were refined from the observed positions of all strong reflections in each data set. A Gaussian grid face-indexed with a beam profile was applied for all structures.[34] The structures were solved using SHELXT;[35] the data sets were refined by full-matrix least squares on all unique F^2 values,[35] with anisotropic displacement parameters for all non-hydrogen atoms and with constrained riding hydrogen geometries; U_{iso}(H) was set at 1.2 (1.5 for methyl groups) times U_{eq} of the parent atom. The largest features in the final difference syntheses were close to those of heavy atoms and were of no chemical significance. CrysAlisPro[34] was used for control and integration, and SHELX[35,36] was employed through OLEX2[37] for structure solution and refinement. ORTEP-3[38] and POV-Ray[39] were employed for molecular graphics (see Tables S3 and S4 for key metrical data and Figures S51−S59). Elemental analysis (C, H) was carried out by Mr. Martin Jennings and Mrs. Anne Davies at the Microanalytical Service, School of Chemistry, the University of Manchester. Elemental analysis results for **2-Sm** were inconsistent with the expected values; therefore, a direct titration for lanthanide content[40] was used and showed good agreement between calculated and measured percent Sm content. Low carbon values were obtained consistently for all complexes by elemental analysis, which we attribute to silicon carbide formation as a result of combustion[41] and nonsystematic loss of coordinated THF as implied by our solution stability observations. However, titrations on **1-Sm**, **1-Yb**, **2-Sm**, and **2-Yb** confirm the anticipated percent Ln content for all complexes.

Anhydrous $MgBr_2$ and CaI_2 were purchased from Merck and Alfa Aesar, respectively, and were used as received. The complexes [LnI$_2$(THF)$_2$] (Ln = Sm, Eu, Yb)[22] and [Mg(Si^{t}Bu$_3$)$_2$(THF)$_2$] (**1-Mg**)[21d] were prepared according to literature procedures; Na-Si^{t}Bu$_2$Me[24] and NaSi^{t}Bu$_3$[23] were prepared by adapted literature

https://doi.org/10.1021/jacs.1c03236
J. Am. Chem. Soc. 2021, 143, 9813−9824

procedures, and these modifications are detailed in the Supporting Information.[25]

Computational Methods. The Gaussian 16 software package, revision C.01,[42] was used for all DFT calculations, excluding those used to calculate NMR spectroscopy parameters (see below and Tables S5−S10 and Figures S60−S82). The hybrid density functional approximation PBE0[29,43] was employed. Dispersion was considered with Grimme's D3 dispersion corrections and the Becke−Johnson damping parameters (D3-BJ)[44−48] in all systems, except for No, where these corrections are not available. Dunning's correlation consistent basis sets of polarized triple-ζ quality were used for H, C, N, O, and Si atoms,[49−52] and Pople's 6-311G* basis set for Ca and K.[53] Stuttgart−Bonn small-core relativistic pseudopotentials and associate segmented basis sets were used for the Sm, Eu, Yb, and No atoms.[54−58] Initial geometries were taken from the single-crystal XRD structures, where available, and optimized with no symmetry constraints. The quadratically convergent SCF procedure (SCF = XQC) was used in the case of the Sm compounds to assist with the electronic convergence. Otherwise, default settings used for the optimization and analysis of the harmonic vibrational frequencies confirmed that energetic minima were located. In the systems where pseudopotentials were employed, single-point energy calculations were subsequently performed with the all-electron SARC basis sets for the metals,[54,59,60] including the second-order Douglas−Kroll−Hess (DKH2) Hamiltonian to account for scalar relativistic effects.[61−63] Bonding analyses were performed on the all-electron electronic structures.

The natural bond orbital (NBO 7.0) software package,[64,65] integrated with Gaussian 16, was used to compute natural localized molecular orbitals (NLMOs) and natural population analysis of the Ln−silicon bonding orbitals. WFX files generated from Gaussian 16 were used for the QCT analysis, including QTAIM and IQA analysis, which was performed with the AIMAll software package.[66] The IQA analysis was implemented using encomp = 4, and the WFX file was edited to include the appropriate ⟨Model⟩ tag.

NMR chemical shifts were computed with the Amsterdam density functional theory (ADF) program.[67,68] Spin−orbit coupled, single-point calculations, using the optimized geometries described above, employed the PBE0 hybrid and SAOP functionals. All-electron Slater-type orbital triple-ζ-quality basis sets (TZ2P) were employed for the Mg, Ca, Yb, No, and Si atoms, and double-ζ-quality basis sets (DZP) were employed for all other atoms, in conjunction with the two-component zero-order regular approximation (ZORA) Hamiltonian.[69−71] The ^{29}Si NMR chemical shifts are reported relative to tetramethylsilane (TMS).

General Procedure for the Synthesis of 1-Ln and 2-Ln. A mixture of $[LnI_2(THF)_2]$ and 2 equiv of $NaSiR_3$ in a Schlenk flask was cooled to −78 °C, and THF (10 mL/mmol) was added. The reaction mixture was warmed to room temperature and stirred for 18 h. Volatiles were removed in vacuo, and the product was extracted into hexane (25 mL/mmol) and filtered. Concentration of the resultant solution and storage at 5 °C overnight resulted in the formation of crystals of the product, with further crops obtained at −25 °C.

$[Ca(Si^tBu_3)_2(THF)_2]$ ***(1-Ca).*** A Schlenk flask charged with $CaBr_2$ (0.400 g, 2 mmol) and $NaSi^tBu_3$ (0.890 g, 4 mmol) was cooled to −78 °C, and THF (35 mL) was added. The resulting amber reaction mixture was warmed to room temperature and stirred for 18 h. Volatiles were removed *in vacuo*, and the product was extracted into heptane (50 mL). Removal of heptane under reduced pressure gave crude **1-Ca** as a pale yellow solid (0.518 g, 0.89 mmol, 44%). Pale yellow needles suitable for single-crystal XRD were obtained from a concentrated heptane solution stored at −25 °C. Anal. Calcd for $C_{32}H_{70}CaO_2Si_2$: C, 65.91; H, 12.10. Found: C, 64.72; H, 12.15. ^{1}H NMR (400.07 MHz, C_6D_6, 298 K): δ 1.26 (m, 8H, CH_2), 1.41 (s, 54H, $C(CH_3)_3$), 3.59 (m, 8H, OCH_2). $^{13}C\{^1H\}$ NMR (100.60 MHz, C_6D_6, 298 K): δ 24.85 (CH_2), 25.12 (CH_2), 31.24 ($C(CH_3)_3$), 31.57 ($C(CH_3)_3$), 34.66 ($C(CH_3)_3$), 69.33 (OCH_2). $^{29}Si\{^1H\}$ NMR (79.48 MHz, C_6D_6, 298 K): δ 25.64. ATR-IR: $\tilde{\nu}$ 2967 (w), 2878 (w), 2832 (m), 1471 (m), 1026 (w), 871 (w), 806 (m), 566 (w).

$[Sm(Si^tBu_3)_2(THF)_3]$ ***(1-Sm).*** This complex was prepared according to the general procedure with $[SmI_2(THF)_2]$ (1.097 g, 2 mmol) and $NaSi^tBu_3$ (0.890 g, 4 mmol); **1-Sm** was obtained as dark purple crystals (0.493 g, 0.64 mmol, 32%). Anal. Calcd for $C_{36}H_{78}O_3Si_2Sm$: C, 56.48; H, 10.27; Sm, 19.64. Found: C, 52.83; H, 10.36; Sm, 20.22. μ_{eff} = 3.40 μ_B (Evans method). ^{1}H NMR (400.07 MHz, C_6D_6/C_4D_8O, 298 K): δ −1.55 (s, br, $\nu_{1/2}$ ≈ 10 Hz, 54H, $C(CH_3)_3$), 1.48 (m, br, $\nu_{1/2}$ ≈ 10 Hz, 12H, CH_2), 3.91 (m, br, $\nu_{1/2}$ ≈ 10 Hz, 12H, OCH_2). The $^{13}C\{^1H\}$ NMR spectrum could not be assigned, and no resonances were detected in the $^{29}Si\{^1H\}$ NMR spectrum due to the paramagnetism of **1-Sm**. ATR-IR: $\tilde{\nu}$ 2964 (w), 2828 (m), 1471 (m), 1377 (w), 1023 (m), 867 (m), 806 (m), 569 (m) cm^{-1}.

$[Eu(Si^tBu_3)_2(THF)_3]$ ***(1-Eu).*** This complex was prepared according to the general procedure with $[EuI_2(THF)_2]$ (1.100 g, 2 mmol) and $NaSi^tBu_3$ (0.890 g, 4 mmol); **1-Eu** was obtained as yellow crystals (0.489 g, 0.64 mmol, 32%). Anal. Calcd for $C_{36}H_{78}EuO_3Si_2$: C, 56.36; H, 10.25. Found: C, 51.02; H, 9.70. μ_{eff} = 8.17 μ_B (Evans method). ^{1}H NMR (400.07 MHz, C_6D_6/C_4D_8O, 298 K): −3.87 (s, br, $\nu_{1/2}$ ≈ 2,350 Hz, $C(CH_3)_3$), 1.39 (m, br, $\nu_{1/2}$ ≈ 270 Hz, CH_2), 3.58 (m, br, $\nu_{1/2}$ ≈ 360 Hz, OCH_2). No resonances were observed in the $^{13}C\{^1H\}$ and $^{29}Si\{^1H\}$ NMR spectra due to the paramagnetism of **1-Eu**. FTIR: $\tilde{\nu}$ 2918 (w), 2834 (m), 1467 (m), 1026 (m), 869 (m), 808 (m), 752 (m), 647 (m) cm^{-1}.

$[Yb(Si^tBu_3)_2(THF)_2]$ ***(1-Yb).*** This complex was prepared according to the general procedure with $[YbI_2(THF)_2]$ (1.142 g, 2 mmol) and $NaSi^tBu_3$ (0.890 g, 4 mmol); **1-Yb** was obtained as orange crystals (0.608 g, 0.85 mmol, 42%). Anal. Calcd for $C_{32}H_{70}O_2Si_2Yb$: C, 53.67; H, 9.85; Yb, 24.17. Found: C, 50.43; H, 9.53; Yb, 24.53. ^{1}H NMR (500.19 MHz, C_6D_6/C_4D_8O, 298 K): δ 1.37 (s, 54H, $C(CH_3)_3$), 1.45 (m, 8H, CH_2), 3.56 (m, 8H, OCH_2). $^{13}C\{^1H\}$ NMR (125.77 MHz, C_6D_6/C_4D_8O, 298 K): δ 26.06 (CH_2), 26.12 ($C(CH_3)_3$), 34.71 ($C(CH_3)_3$), 68.21 (OCH_2). $^{29}Si\{^1H\}$ NMR (79.48 MHz, C_6D_6/C_4D_8O, 298 K): 54.19 ($^1J_{Yb-Si}$ = 976 Hz). $^{171}Yb\{^1H\}$ NMR (87.52 MHz, C_6D_6/C_4D_8O, 298 K): 1044.64 ($^1J_{Yb-Si}$ = 976 Hz). ATR-IR: $\tilde{\nu}$ 2961 (w), 2828 (m), 1467 (m), 1378 (w), 1023 (m), 869 (m), 806 (m), 567 (m) cm^{-1}.

$[Mg(Si^tBu_2Me)_2(THF)_2]$ ***(2-Mg).*** A Schlenk flask charged with $MgBr_2$ (0.921 g, 5 mmol) and $NaSi^tBu_2Me$ (1.803 g, 10 mmol) was cooled to −78 °C, and THF (40 mL) was added. The resulting beige reaction mixture was warmed to room temperature and stirred for 18 h. Volatiles were removed *in vacuo*, and the product was extracted into heptane (50 mL). Removal of heptane under reduced pressure gave crude **2-Mg** as a colorless solid (1.200 g, 2.48 mmol, 49%). Colorless needles suitable for single-crystal XRD were obtained from a concentrated heptane solution stored at −25 °C. Anal. Calcd for $C_{26}H_{56}O_2Si_2Mg$: C, 64.90; H, 11.73. Found: C, 61.96; H, 12.23. Consistently low carbon values were obtained and attributed to silicon carbide formation. ^{1}H NMR (400.07 MHz, C_6D_6, 298 K): δ 0.26 (s, 6H, CH_3), 1.26 (m, 8H, CH_2), 1.32 (s, 36H, $C(CH_3)_3$), 3.58 (m, 8H, OCH_2). $^{13}C\{^1H\}$ NMR (100.60 MHz, C_6D_6, 298 K): δ −1.06 (CH_3), 21.99 ($C(CH_3)_3$), 25.48 (CH_2), 32.18 ($C(CH_3)_3$), 69.92 (OCH_2). $^{29}Si\{^1H\}$ NMR (79.48 MHz, C_6D_6, 298 K): δ 4.51. ATR-IR: $\tilde{\nu}$ 2914 (w), 2879 (w), 2838 (m), 1465 (m), 1032 (m), 873 (m), 814 (m), 754 (m), 645 (m), 577 (m) cm^{-1}.

$[Ca(Si^tBu_2Me)_2(THF)_3]$ ***(2-Ca).*** A Schlenk flask charged with $CaBr_2$ (0.400 g, 3 mmol) and $NaSi^tBu_2Me$ (0.721 g, 4 mmol) was cooled to −78 °C, and THF (35 mL) was added. The resulting yellow reaction mixture was warmed to room temperature and stirred for 18 h. Volatiles were removed *in vacuo*, and the product was extracted into heptane (50 mL). Removal of heptane under reduced pressure gave crude **2-Ca** as a colorless solid (0.468 g, 0.82 mmol, 41%). Colorless needles suitable for single-crystal XRD were obtained from a concentrated heptane solution stored at −25 °C. Anal. Calcd for $C_{30}H_{66}CaO_3Si_2$: C, 63.09; H, 11.65. Found: C, 61.99; H, 11.89. ^{1}H NMR (400.07 MHz, C_6D_6, 298 K): δ 0.29 (s, 6H, CH_3), 1.32 (m, 12H, CH_2), 1.34 (s, 36H, $C(CH_3)_3$), 3.61 (m, 12H, OCH_2). $^{13}C\{^1H\}$ NMR (100.60 MHz, C_6D_6, 298 K): δ −0.17 (CH_3), 22.17 ($C(CH_3)_3$), 25.51 (CH_2), 32.62 ($C(CH_3)_3$), 68.92 (OCH_2). $^{29}Si\{^1H\}$ NMR (79.48 MHz, C_6D_6, 298 K): δ 3.06. ATR-IR: $\tilde{\nu}$ 2932 (w), 2867

https://doi.org/10.1021/jacs.1c03236
J. Am. Chem. Soc. 2021, 143, 9813−9824

(w), 2828 (m), 1463 (w), 1030 (m), 872 (m), 813 (m), 759 (m), 632 (m), 570 (w) cm^{-1}.

*[Sm(Si^{t}Bu$_2$Me)$_2$(THF)$_3$] (**2-Sm**).* This complex was prepared according to the general procedure with [$SmI_2(THF)_2$] (2.742 g, 5 mmol) and NaSi^{t}Bu$_2$Me (1.803 g, 10 mmol); **2-Sm** was obtained as dark purple crystals (1.511 g, 2.22 mmol, 44%). Anal. Calcd for $C_{30}H_{66}O_3Si_2Sm$: C, 52.88; H, 9.76; Sm, 22.07. Found: C, 44.58; H, 8.64; Sm, 21.93. μ_{eff} = 3.41 μ_B (Evans method). ^{1}H NMR (400.07 MHz, C_6D_6/C_4D_8O, 298 K): δ −11.20 (s, br, $\nu_{1/2} \approx$ 30 Hz, 6H, CH_3), −0.40 (s, br, $\nu_{1/2} \approx$ 30 Hz, 36H, $C(CH_3)_3$), 1.47 (m, br, $\nu_{1/2} \approx$ 30 Hz, 12H, CH_2), 3.65 (m, br, $\nu_{1/2} \approx$ 30 Hz, 12H, OCH_2). The $^{13}C\{^1H\}$ NMR spectrum could not be assigned, and no resonances were detected in the $^{29}Si\{^1H\}$ NMR spectrum due to the paramagnetism of **2-Sm**. ATR-IR: $\tilde{\nu}$ 2922 (w), 2857 (w), 2830 (m), 1463 (m), 1260 (m), 1028 (m), 867 (m), 810 (m), 754 (m), 625 (m) cm^{-1}.

*[Eu(Si^{t}Bu$_2$Me)$_2$(THF)$_3$] (**2-Eu**).* This complex was prepared according to the general procedure with [$EuI_2(THF)_2$] (1.100 g, 2 mmol) and NaSi^{t}Bu$_2$Me (0.721 g, 4 mmol); **2-Eu** was obtained as yellow crystals (0.632 g, 0.93 mmol, 46%). Anal. Calcd for $C_{30}H_{66}EuO_3Si_2$: C, 52.76; H, 9.74. Found: C, 48.52; H, 9.92. μ_{eff} = 7.89 μ_B (Evans method). ^{1}H NMR (400.07 MHz, C_6D_6/C_4D_8O, 298 K): −23.83 (s, br, $\nu_{1/2} \approx$ 2,750 Hz, CH_3), −3.25 (s, br, $\nu_{1/2} \approx$ 2,100 Hz, $C(CH_3)_3$), 1.28 (m, br, $\nu_{1/2} \approx$ 250 Hz, CH_2), 3.62 (m, br, $\nu_{1/2} \approx$ 420 Hz, OCH_2). No resonances were observed in the $^{13}C\{^1H\}$ and $^{29}Si\{^1H\}$ NMR spectra due to the paramagnetism of **2-Eu**. ATR-IR: $\tilde{\nu}$ 2904 (w), 2869 (w), 2830 (m), 1457 (m), 1030 (m), 875 (m), 810 (m), 752 (m), 625 (m) cm^{-1}.

*[Yb(Si^{t}Bu$_2$Me)$_2$(THF)$_3$] (**2-Yb**).* This complex was prepared according to the general procedure with [$YbI_2(THF)_2$] (1.142 g, 2 mmol) and NaSi^{t}Bu$_2$Me (0.721 g, 4 mmol); **2-Yb** was obtained as orange crystals from a concentrated pentane solution (0.504 g, 0.72 mmol, 36%). Anal. Calcd for $C_{30}H_{66}O_3Si_2Yb$: C, 51.18; H, 9.45; Yb, 24.58. Found: C, 48.84; H, 9.31; Yb, 25.89. ^{1}H NMR (400.07 MHz, C_6D_6/C_4D_8O, 298 K): δ 0.19 (s, 6H, CH_3), 1.23 (s, 36H, $C(CH_3)_3$), 1.47 (m, 12H, CH_2), 3.56 (m, 12H, OCH_2). $^{13}C\{^1H\}$ NMR (125.77 MHz, C_6D_6/C_4D_8O, 298 K): δ 0.68 (CH_3), 23.53 ($C(CH_3)_3$), 26.12 (CH_2), 32.69 ($C(CH_3)_3$), 68.21 (OCH_2). $^{29}Si\{^1H\}$ NMR (79.48 MHz, C_6D_6/C_4D_8O, 298 K): 29.24 ($^1J_{Yb-Si}$ = 921 Hz). $^{171}Yb\{^1H\}$ NMR (87.52 MHz, C_6D_6/C_4D_8O, 298 K): 825.07 ($^1J_{Yb-Si}$ = 921 Hz). ATR-IR: 2910 (w), 2863 (w), 2830 (m), 1463 (m), 1032 (m), 869 (m), 810 (m), 754 (m), 627 (m) cm^{-1}.

■ ASSOCIATED CONTENT

Supporting Information

The Supporting Information is available free of charge at https://pubs.acs.org/doi/10.1021/jacs.1c03236.

Additional experimental details for physical and computational data associated with this manuscript (PDF)

Accession Codes

CCDC 2061770−2061780 contain the supplementary crystallographic data for this paper. These data can be obtained free of charge via www.ccdc.cam.ac.uk/data_request/cif, or by emailing data_request@ccdc.cam.ac.uk, or by contacting The Cambridge Crystallographic Data Centre, 12 Union Road, Cambridge CB2 1EZ, UK; fax: +44 1223 336033.

■ AUTHOR INFORMATION

Corresponding Authors

Nikolas Kaltsoyannis − *Department of Chemistry, The University of Manchester, Manchester M13 9PL, U.K.;* orcid.org/0000-0003-0293-5742; Email: nikolas.kaltsoyannis@manchester.ac.uk

David P. Mills − *Department of Chemistry, The University of Manchester, Manchester M13 9PL, U.K.;* orcid.org/0000-0003-1575-7754; Email: david.mills@manchester.ac.uk

Stephen T. Liddle − *Department of Chemistry, The University of Manchester, Manchester M13 9PL, U.K.;* orcid.org/0000-0001-9911-8778; Email: steve.liddle@manchester.ac.uk

Authors

Benjamin L. L. Réant − *Department of Chemistry, The University of Manchester, Manchester M13 9PL, U.K.;* orcid.org/0000-0002-8137-5298

Victoria E. J. Berryman − *Department of Chemistry, The University of Manchester, Manchester M13 9PL, U.K.*

Annabel R. Basford − *Department of Chemistry, The University of Manchester, Manchester M13 9PL, U.K.*

Lydia E. Nodaraki − *Department of Chemistry, The University of Manchester, Manchester M13 9PL, U.K.*

Ashley J. Wooles − *Department of Chemistry, The University of Manchester, Manchester M13 9PL, U.K.;* orcid.org/0000-0001-7411-9627

Floriana Tuna − *Department of Chemistry, The University of Manchester, Manchester M13 9PL, U.K.*

Complete contact information is available at: https://pubs.acs.org/10.1021/jacs.1c03236

Notes

The authors declare no competing financial interest.

■ ACKNOWLEDGMENTS

We thank the University of Manchester for a PhD studentship for B.L.L.R. (Nuclear Endowment), a postdoctoral fellowship to V.E.J.B., and access to the Computational Shared Facility and the Engineering and Physical Sciences Research Council (EPSRC) (EP/R002605X/1, EP/P001386/1, EP/M027015/1, and EP/N022122/1) and European Research Council (CoG-816268 and CoG-612724) for funding. We thank the EPSRC UK National Electron Paramagnetic Resonance Service for access to the EPR facility and Mr. Carlo Bawn and Dr. Ralph Adams at the University of Manchester School of Chemistry NMR service for assisting with ^{171}Yb NMR spectroscopic measurements. Additional research data supporting this publication are available from Figshare at https://doi.org/10.6084/m9.figshare.14269367.v2.

■ REFERENCES

(1) Pauling, L. The Nature of the Chemical Bond. Application of Results Obtained from the Quantum Mechanics and from a Theory of Paramagnetic Susceptibility to the Structure of Molecules. *J. Am. Chem. Soc.* **1931**, *53* (4), 1367−1400.

(2) Choppin, G. R. Covalency in f-Element Bonds. *J. Alloys Compd.* **2002**, *344*, 55−59.

(3) (a) Kaltsoyannis, N. Does Covalency Increase or Decrease across the Actinide Series? Implications for Minor Actinide Partitioning. *Inorg. Chem.* **2013**, *52* (7), 3407−3413. (b) Neidig, M. L.; Clark, D. L.; Martin, R. L. Covalency in f-Element Complexes. *Coord. Chem. Rev.* **2013**, *257* (2), 394−406.

(4) (a) Kirker, I.; Kaltsoyannis, N. Does covalency *really* increase across the 5f series? A comparison of molecular orbital, natural population, spin and electron density analyses of $AnCp_3$ (An = Th-Cm; Cp = C_5H_5). *Dalton Trans.* **2011**, *40* (1), 124−131. (b) Walensky, J. R.; Martin, R. L.; Ziller, J. W.; Evans, W. J. Importance of Energy Level Matching for Bonding in Th^{3+}-Am^{3+} Actinide Metallocene Amidinates, $(C_5Me_5)_2[^iPrNC(Me)N^iPr]An$.

Inorg. Chem. **2010**, *49* (21), 10007−10012. (c) Tassell, M. J.; Kaltsoyannis, N. Covalency in $AnCp_4$ (An = Th-Cm): a comparison of molecular orbital, natural population and atoms-in-molecules analyses. *Dalton Trans.* **2010**, *39* (29), 6719−6725.

(5) (a) Baker, M. L.; Mara, M. W.; Yan, J. J.; Hodgson, K. O.; Hedman, B.; Solomon, E. I. K- and L-edge X-ray absorption spectroscopy (XAS) and resonant inelastic X-ray scattering (RIXS) determination of differential orbital covalency (DOC) of transition metal sites. *Coord. Chem. Rev.* **2017**, *345*, 182−208. (b) Denecke, M. A. Synchrotron Applications to f-Element Research in the Nuclear Fuel Cycle. *Dalton Trans.* **2015**, *44* (6), 2606−2612. (c) Solomon, E. I.; Hedman, B.; Hodgson, K. O.; Dey, A.; Szilagyi, R. K. Ligand K-Edge X-Ray Absorption Spectroscopy: Covalency of Ligand-Metal Bonds. *Coord. Chem. Rev.* **2005**, *249*, 97−129.

(6) Su, J.; Batista, E. R.; Boland, K. S.; Bone, S. E.; Bradley, J. A.; Cary, S. K.; Clark, D. L.; Conradson, S. D.; Ditter, A. S.; Kaltsoyannis, N.; Keith, J. M.; Kerridge, A.; Kozimor, S. A.; Löble, M. W.; Martin, R. L.; Minasian, S. G.; Mocko, V.; La Pierre, H. S.; Seidler, G. T.; Shuh, D. K.; Wilkerson, M. P.; Wolfsberg, L. E.; Yang, P. Energy-Degeneracy-Driven Covalency in Actinide Bonding. *J. Am. Chem. Soc.* **2018**, *140* (51), 17977−17984. (b) Kerridge, A. Quantification of f-Element Covalency through Analysis of the Electron Density: Insights from Simulation. *Chem. Commun.* **2017**, *53* (50), 6685−6695. (c) Cross, J. N.; Su, J.; Batista, E. R.; Cary, S. K.; Evans, W. J.; Kozimor, S. A.; Mocko, V.; Scott, B. L.; Stein, B. W.; Windorff, C. J.; Yang, P. Covalency in Americium(III) Hexachloride. *J. Am. Chem. Soc.* **2017**, *139* (25), 8667−8677.

(7) (a) Roessler, M. M.; Salvadori, E. Principles and Applications of EPR Spectroscopy in the Chemical Sciences. *Chem. Soc. Rev.* **2018**, *47* (8), 2534−2553. (b) Formanuik, A.; Ariciu, A.-M.; Ortu, F.; Beekmeyer, R.; Kerridge, A.; Tuna, F.; McInnes, E. J. L.; Mills, D. P. Actinide Covalency Measured by Pulsed Electron Paramagnetic Resonance Spectroscopy. *Nat. Chem.* **2017**, *9* (6), 578−583.

(8) Vĺcha, J.; Novotný, J.; Komorovsky, S.; Straka, M.; Kaupp, M.; Marek, R. Relativistic Heavy-Neighbor-Atom Effects on NMR Shifts: Concepts and Trends across the Periodic Table. *Chem. Rev.* **2020**, *120* (15), 7065−7103.

(9) Hrobárik, P.; Hrobáriková, V.; Greif, A. H.; Kaupp, M. Giant Spin-Orbit Effects on NMR Shifts in Diamagnetic Actinide Complexes: Guiding the Search of Uranium(VI) Hydride Complexes in the Correct Spectral Range. *Angew. Chem., Int. Ed.* **2012**, *51* (43), 10884−10888.

(10) (a) Panetti, G. B.; Sergentu, D.-C.; Gau, M. R.; Carroll, P. J.; Autschbach, J.; Walsh, P. J.; Schelter, E. J. Isolation and characterization of a covalent Ce^{IV}-Aryl complex with an anomalous ^{13}C chemical shift. *Nat. Commun.* **2021**, *12*, 21766. (b) Mullane, K. C.; Hrobárik, P.; Cheisson, T.; Manor, B. C.; Carroll, P. J.; Schelter, E. J. ^{13}C NMR Shifts as an Indicator of U-C Bond Covalency in Uranium(VI) Acetylide Complexes: An Experimental and Computational Study. *Inorg. Chem.* **2019**, *58* (7), 4152−4163. (c) Smiles, D. E.; Wu, G.; Hrobárik, P.; Hayton, T. W. Synthesis, Thermochemistry, Bonding, and ^{13}C NMR Chemical Shift Analysis of a Phosphorano-Stabilized Carbene of Thorium. *Organometallics* **2017**, *36* (23), 4519−4524. (d) Seaman, L. A.; Hrobárik, P.; Schettini, M. F.; Fortier, S.; Kaupp, M.; Hayton, T. W. A Rare Uranyl(VI)-Alkyl Ate Complex $[Li(DME)_{1.5}]_2[UO_2(CH_2SiMe_3)_4]$ and Its Comparison with a Homoleptic Uranium(VI)-Hexaalkyl. *Angew. Chem., Int. Ed.* **2013**, *52* (11), 3259−3263.

(11) Staun, S. L.; Sergentu, D. C.; Wu, G.; Autschbach, J.; Hayton, T. W. Use of ^{15}N NMR Spectroscopy to Probe Covalency in a Thorium Nitride. *Chem. Sci.* **2019**, *10* (26), 6431−6436.

(12) Wu, W.; Rehe, D.; Hrobárik, P.; Kornienko, A. Y.; Emge, T. J.; Brennan, J. G. Molecular Thorium Compounds with Dichalcogenide Ligands: Synthesis, Structure, ^{77}Se NMR Study, and Thermolysis. *Inorg. Chem.* **2018**, *57*, 14821−14833.

(13) Smiles, D. E.; Wu, G.; Hrobárik, P.; Hayton, T. W. Use of ^{77}Se and ^{125}Te NMR Spectroscopy to Probe Covalency of the Actinide-Chalcogen Bonding in $[Th(En)\{N(SiMe_3)_2\}_3]^-$ (E = Se, Te; N = 1, 2) and Their Oxo-Uranium(VI) Congeners. *J. Am. Chem. Soc.* **2016**, *138* (3), 814−825.

(14) Sergentu, D. C.; Kent, G. T.; Staun, S. L.; Yu, X.; Cho, H.; Autschbach, J.; Hayton, T. W. Probing the Electronic Structure of a Thorium Nitride Complex by Solid-State ^{15}N NMR Spectroscopy. *Inorg. Chem.* **2020**, *59* (14), 10138−10145.

(15) (a) Martel, L.; Magnani, N.; Vigier, J. F.; Boshoven, J.; Selfslag, C.; Farnan, I.; Griveau, J. C.; Somers, J.; Fanghänel, T. High-Resolution Solid-State Oxygen-17 NMR of Actinide-Bearing Compounds: An Insight into the 5f Chemistry. *Inorg. Chem.* **2014**, *53* (13), 6928−6933. (b) Cho, H.; De Jong, W. A.; Soderquist, C. Z. Probing the Oxygen Environment in UO_2^{2+} by Solid-State ^{17}O Nuclear Magnetic Resonance Spectroscopy and Relativistic Density Functional Calculations. *J. Chem. Phys.* **2010**, *132* (8), 084501.

(16) (a) Devore, M. A.; Klug, C. A.; Kriz, M. R.; Roy, L. E.; Wellons, M. S. Investigations of Uranyl Fluoride Sesquihydrate ($UO_2F_2 \cdot 1.57H_2O$): Combining ^{19}F Solid-State MAS NMR Spectroscopy and GIPAW Chemical Shift Calculations. *J. Phys. Chem. A* **2018**, *122* (34), 6873−6878. (b) Martel, L.; Capelli, E.; Body, M.; Klipfel, M.; Beneš, O.; Maksoud, L.; Raison, P. E.; Suard, E.; Visscher, L.; Bessada, C.; Legein, C.; Charpentier, T.; Kovács, A. Insight into the Crystalline Structure of ThF_4 with the Combined Use of Neutron Diffraction, ^{19}F Magic-Angle Spinning-NMR, and Density Functional Theory Calculations. *Inorg. Chem.* **2018**, *57* (24), 15350−15360.

(17) (a) Réant, B. L. L.; Liddle, S. T.; Mills, D. P. F-Element Silicon and Heavy Tetrel Chemistry. *Chem. Sci.* **2020**, *11* (40), 10871−10886. (b) Marschner, C. Silicon-Centered Anions. In *Organosilicon Compounds: Theory and Experiment (Synthesis)*; Elsevier: 2017; pp 295−360.

(18) (a) Bursch, M.; Gasevic, T.; Stückrath, J. B.; Grimme, S. Comprehensive Benchmark Study on the Calculation of ^{29}Si NMR Chemical Shifts. *Inorg. Chem.* **2021**, *60*, 272. (b) Huynh, W.; Conley, M. P. Origin of the ^{29}Si NMR Chemical Shift in R_3Si-X and Relationship to the Formation of Silylium (R_3Si^+) Ions. *Dalton Trans.* **2020**, *49* (45), 16453−16463. (c) Zhang, C.; Patschinski, P.; Stephenson, D. S.; Panisch, R.; Wender, J. H.; Holthausen, M. C.; Zipse, H. The Calculation of ^{29}Si NMR Chemical Shifts of Tetracoordinated Silicon Compounds in the Gas Phase and in Solution. *Phys. Chem. Chem. Phys.* **2014**, *16* (31), 16642−16650. (d) Truflandier, L. A.; Brendler, E.; Wagler, J.; Autschbach, J. ^{29}Si DFT/NMR Observation of Spin-Orbit Effect in Metallasilatrane Sheds Some Light on the Strength of the Metal→silicon Interaction. *Angew. Chem., Int. Ed.* **2011**, *50* (1), 255−259.

(19) Réant, B. L. L.; Berryman, V.; Seed, J.; Basford, A.; Formanuik, A.; Wooles, A.; Kaltsoyannis, N.; Liddle, S.; Mills, D. P. Polarised Covalent Thorium(IV)- and Uranium(IV)-Silicon Bonds. *Chem. Commun.* **2020**, *56* (83), 12620−12623.

(20) (a) Lampland, N. L.; Pindwal, A.; Yan, K.; Ellern, A.; Sadow, A. D. Rare Earth and Main Group Metal Poly(Hydrosilyl) Compounds. *Organometallics* **2017**, *36*, 4546−4557. (b) Zitz, R.; Hlina, J.; Aghazadeh Meshgi, M.; Krenn, H.; Marschner, C.; Szilvási, T.; Baumgartner, J. Using Functionalized Silyl Ligands To Suppress Solvent Coordination to Silyl Lanthanide(II) Complexes. *Inorg. Chem.* **2017**, *56* (9), 5328−5341. (c) Aghazadeh Meshgi, M.; Zitz, R.; Walewska, M.łg.; Baumgartner, J.; Marschner, C. Tuning the Si-N Interaction in Metalated Oligosilanylsilatranes. *Organometallics* **2017**, *36* (7), 1365−1371. (d) Zitz, R.; Hlina, J.; Gatterer, K.; Marschner, C.; Szilvási, T.; Baumgartner, J. Neutral 'Cp-Free' Silyl-Lanthanide(II) Complexes: Synthesis, Structure, and Bonding Analysis. *Inorg. Chem.* **2015**, *54* (14), 7065−7072. (e) Niemeyer, M. Reactions of Hypersilyl Potassium with Rare-Earth Metal Bis(Trimethylsilylamides): Addition versus Peripheral Deprotonation. *Inorg. Chem.* **2006**, *45* (22), 9085−9095. (f) Corradi, M. M.; Frankland, A. D.; Hitchcock, P. B.; Lappert, M. F.; Lawless, G. A. Synthesis, Structure and Reactivity of $[Yb(\eta\text{-}C_5Me_5)\{Si(SiMe_3)_3\}(THF)_2]$. *Chem. Commun.* **1996**, 2323−2324. (g) Bochkarev, L. N.; Makarov, V. M.; Hrzhanovskaya, Y. N.; et al. Synthesis and Structure of Organosilicon and Organogermanium Complexes of Ytterbium $(Ph_3E)_2Yb(THF)_4$ with Yb-Si and Yb-Ge Bonds. *J. Organomet. Chem.* **1994**, *467*, C3−C5.

https://doi.org/10.1021/jacs.1c03236
J. Am. Chem. Soc. 2021, 143, 9813−9824

(21) (a) Lemmerz, L. E.; Leich, V.; Martin, D.; Spaniol, T. P.; Okuda, J. Silyl-Hydrosilane Exchange at a Magnesium Triphenylsilyl Complex Supported by a Cyclen-Derived NNNN-Type Macrocyclic Ligand. *Inorg. Chem.* **2017**, *56* (24), 14979−14990. (b) Leich, V.; Spaniol, T. P.; Maron, L.; Okuda, J. Hydrosilylation Catalysis by an Earth Alkaline Metal Silyl: Synthesis, Characterization, and Reactivity of Bis(Triphenylsilyl)Calcium. *Chem. Commun.* **2014**, *50* (18), 2311−2314. (c) Teng, W.; Ruhlandt-Senge, K. Syntheses and Structures of the First Heavy Alkaline Earth Metal Bis(Tris(Trimethylsilyl))-Silanides. *Organometallics* **2004**, *23* (11), 2694−2700. (d) Lerner, H.-W.; Scholz, S.; Bolte, M.; Wiberg, N.; Nöth, H.; Krossing, I. Synthesis and Structures of Alkaline-Earth Metal Supersilanides: $^{t}Bu_3SiMX$ and $^{t}Bu_3Si\text{-}M\text{-}Si^{t}Bu_3$ (M = Be, Mg; X = Cl, Br). *Eur. J. Inorg. Chem.* **2003**, *2003* (4), 666−670. (e) Farwell, J. D.; Lappert, M. F.; Marschner, C.; Strissel, C.; Tilley, T. D. The First Structurally Characterised Oligosilylmagnesium Compound. *J. Organomet. Chem.* **2000**, *603* (2), 185−188.

(22) Girard, P.; Namy, J. L.; Kagan, B. Mild Preparation of SmI_2 and YbI_2 and Their Use as Reducing or Coupling Agents. *J. Am. Chem. Soc.* **1980**, *102*, 2693−2698.

(23) Wiberg, N.; Amelunxen, K.; Lerner, H.-W. W.; Schuster, H.; Nöth, H.; Krossing, I.; Schmidt-Amelunxen, M.; Seifert, T. Donorfreie Und Donorhaltige Supersilylalkalimetalle $^{t}Bu_3SiM$: Synthesen, Charakterisierung, Strukturen. *J. Organomet. Chem.* **1997**, *542* (1), 1−18.

(24) Sekiguchi, A.; Fukawa, T.; Nakamoto, M.; Lee, V. Y.; Ichinohe, M. Isolable Silyl and Germyl Radicals Lacking Conjugation with π-Bonds: Synthesis, Characterization, and Reactivity. *J. Am. Chem. Soc.* **2002**, *124* (33), 9865−9869.

(25) See the Supporting Information for further details.

(26) Sänger, I.; Kückmann, T. I.; Dornhaus, F.; Bolte, M.; Wagner, M.; Lerner, H. W. The Inverse Sandwich Complex $[(K(18\text{-Crown-}6))_2Cp][CpFe(CO)_2]$ - Unpredictable Redox Reactions of $[CpFe(CO)_2]I$ with the Silanides $Na[SiR^{t}Bu_2]$ (R = Me, ^{t}Bu) and the Isoelectronic Phosphanyl Borohydride $K[PtBu_2BH_3]$. *Dalton Trans.* **2012**, *41* (22), 6671−6676.

(27) Shannon, R. D. Revised Effective Ionic Radii and Systematic Studies of Interatomic Distances in Halides and Chalcogenides. *Acta Crystallogr., Sect. A: Cryst. Phys., Diffr., Theor. Gen. Crystallogr.* **1976**, *32*, 751−767.

(28) Due to the limited number of reports of ^{171}Yb NMR spectra for silanide complexes, the wide differences in chemical shifts cannot be fully discussed due to unknown methods of calibration or conventional referencing to $[Yb(Cp^*)_2(THF)_2]$. Contemporary referencing methods for ^{171}Yb NMR spectroscopy, which were used for **1-Yb** and **2-Yb**, use the protic frequency of the spectrometer.

(29) Ernzerhof, M.; Scuseria, G. E. Assessment of the Perdew-Burke-Ernzerhof Exchange-Correlation Functional. *J. Chem. Phys.* **1999**, *110* (11), 5029−5036.

(30) (a) Schipper, P. R. T.; Gritsenko, O. V.; Van Gisbergen, S. J. A.; Baerends, E. J. Molecular Calculations of Excitation Energies and (Hyper)Polarizabilities with a Statistical Average of Orbital Model Exchange-Correlation Potentials. *J. Chem. Phys.* **2000**, *112* (3), 1344−1352. (b) Gritsenko, O. V.; Schipper, P. R. T.; Baerends, E. J. Approximation of the Exchange-Correlation Kohn-Sham Potential with a Statistical Average of Different Orbital Model Potentials. *Chem. Phys. Lett.* **1999**, *302* (3−4), 199−207.

(31) Berryman, V. E. J.; Shephard, J. J.; Ochiai, T.; Price, A. N.; Arnold, P. L.; Parsons, S.; Kaltsoyannis, N. Quantum Chemical Topology and Natural Bond Orbital Analysis of M-O Covalency in $M(OC_6H_5)_4$ (M = Ti, Zr, Hf, Ce, Th, Pa, U, Np). *Phys. Chem. Chem. Phys.* **2020**, *22* (29), 16804−16812.

(32) Ramsey, N. F. Magnetic Shielding of Nuclei in Molecules. *Phys. Rev.* **1950**, *78* (6), 699−703.

(33) Kaupp, M.; Malkina, O. L.; Malkin, V. G.; Pyykkö, P. How Do Spin-Orbit-Induced Heavy-Atom Effects on NMR Chemical Shifts Function? Validation of a Simple Analogy to Spin-Spin Coupling by Density Functional Theory (DFT) Calculations on Some Iodo Compounds. *Chem. - Eur. J.* **1998**, *4* (1), 118−126.

(34) *CrysAlisPro*; Agilent Technologies: Yarnton, UK, 2017.

(35) Sheldrick, G. M. SHELXT - Integrated space-group and crystal-structure determination. *Acta Crystallogr., Sect. A: Found. Adv.* **2015**, *71*, 3−8.

(36) Sheldrick, G. M. Crystal Structure Refinement with SHELXL. *Acta Crystallogr., Sect. C: Struct. Chem.* **2015**, *71*, 3−8.

(37) Dolomanov, O. V.; Bourhis, L. J.; Gildea, R. J.; Howard, J. A. K.; Puschmann, H. OLEX2: A Complete Structure Solution, Refinement and Analysis Program. *J. Appl. Crystallogr.* **2009**, *42*, 339−341.

(38) Farrugia, L. J. WinGX and ORTEP for Windows: An Update. *J. Appl. Crystallogr.* **2012**, *45*, 849−854.

(39) *POV-Ray*; Persistence of Vision Raytracer Pty. Ltd.: Williamstown, Australia, 2013.

(40) Hodgson, K. O.; Mares, F.; Starks, D. F.; Streitwieser, A. Lanthanide(III) Complexes with Cyclooctatetraene Dianion. Synthetic Chemistry, Characterization, and Physical Properties. *J. Am. Chem. Soc.* **1973**, *95* (26), 8650−8658.

(41) Hitchcock, P. B.; Lappert, M. F.; Maron, L.; Protchenko, A. V. Lanthanum Does Form Stable Molecular Compounds in the + 2 Oxidation State. *Angew. Chem., Int. Ed.* **2008**, *47*, 1488−1491.

(42) Frisch, M. J.; Trucks, G. W.; Schlegel, H. B.; Scuseria, G. E.; Robb, M. A.; Cheeseman, J. R.; Scalmani, G.; Barone, V.; Petersson, G. A.; Nakatsuji, H.; Li, X.; Caricato, M.; Marenich, A. V.; Bloino, J.; Janesko, B. G.; Gomperts, R.; Mennucci, B.; Hratchian, H. P.; Ortiz, J. V.; Izmaylov, A. F.; Sonnenberg, J. L.; Williams-Young, D.; Ding, F.; Lipparini, F.; Egidi, F.; Goings, J.; Peng, B.; Petrone, A.; Henderson, T.; Ranasinghe, D.; Zakrzewski, V. G.; Gao, J.; Rega, N.; Zheng, G.; Liang, W.; Hada, M.; Ehara, M.; Toyota, K.; Fukuda, R.; Hasegawa, J.; Ishida, M.; Nakajima, T.; Honda, Y.; Kitao, O.; Nakai, H.; Vreven, T.; Throssell, K.; Montgomery, J. A., Jr.; Peralta, J. E.; Ogliaro, F.; Bearpark, M. J.; Heyd, J. J.; Brothers, E. N.; Kudin, K. N.; Staroverov, V. N.; Keith, T. A.; Kobayashi, R.; Normand, J.; Raghavachari, K.; Rendell, A. P.; Burant, J. C.; Iyengar, S. S.; Tomasi, J.; Cossi, M.; Millam, J. M.; Klene, M.; Adamo, C.; Cammi, R.; Ochterski, J. W.; Martin, R. L.; Morokuma, K.; Farkas, O.; Foresman, J. B.; Fox, D. J. *Gaussian 16, Rev. C.01*; Gaussian, Inc.: Wallingford, CT, 2016.

(43) Adamo, C.; Barone, V. Toward Reliable Density Functional Methods without Adjustable Parameters: The PBE0Model. *J. Chem. Phys.* **1999**, *110* (13), 6158−6170.

(44) Grimme, S.; Antony, J.; Ehrlich, S.; Krieg, H. A Consistent and Accurate Ab Initio Parametrization of Density Functional Dispersion Correction (DFT-D) for the 94 Elements H-Pu. *J. Chem. Phys.* **2010**, *132* (15), 154104.

(45) Grimme, S.; Ehrlich, S.; Goerigk, L. Effect of the Damping Function in Dispersion Corrected Density Functional Theory. *J. Comput. Chem.* **2011**, *32* (7), 1456−1465.

(46) Becke, A. D.; Johnson, E. R. Exchange-Hole Dipole Moment and the Dispersion Interaction. *J. Chem. Phys.* **2005**, *122* (15), 154104.

(47) Johnson, E. R.; Becke, A. D. A Post-Hartree-Fock Model of Intermolecular Interactions. *J. Chem. Phys.* **2005**, *123* (2), 024101.

(48) Johnson, E. R.; Becke, A. D. A Post-Hartree-Fock Model of Intermolecular Interactions: Inclusion of Higher-Order Corrections. *J. Chem. Phys.* **2006**, *124* (17), 174104.

(49) Dunning, T. H. J. Gaussian Basis Sets for Use in Correlated Molecular Calculations. I. The Atoms Boron through Neon and Hydrogen. *J. Chem. Phys.* **1989**, *90*, 1007−1023.

(50) Kendall, R. A.; Dunning, T. H.; Harrison, R. J. Electron Affinities of the First-Row Atoms Revisited. Systematic Basis Sets and Wave Functions. *J. Chem. Phys.* **1992**, *96* (9), 6796−6806.

(51) Woon, D. E.; Dunning, T. H. Gaussian Basis Sets for Use in Correlated Molecular Calculations. III. The Atoms Aluminum through Argon. *J. Chem. Phys.* **1993**, *98* (2), 1358−1371.

(52) Wilson, A. K.; Van Mourik, T.; Dunning, T. H. Gaussian Basis Sets for Use in Correlated Molecular Calculations. VI. Sextuple Zeta Correlation Consistent Basis Sets for Boron through Neon. *J. Mol. Struct.: THEOCHEM* **1996**, *388* (1−3), 339−349.

(53) Blaudeau, J. P.; McGrath, M. P.; Curtiss, L. A.; Radom, L. Extension of Gaussian-2 (G2) Theory to Molecules Containing

https://doi.org/10.1021/jacs.1c03236
J. Am. Chem. Soc. 2021, 143, 9813−9824

Third-Row Atoms K and Ca. *J. Chem. Phys.* **1997**, *107* (13), 5016−5021.
(54) Pritchard, B. P.; Altarawy, D.; Didier, B.; Gibson, T. D.; Windus, T. L. New Basis Set Exchange: An Open, Up-to-Date Resource for the Molecular Sciences Community. *J. Chem. Inf. Model.* **2019**, *59* (11), 4814−4820.
(55) Dolg, M.; Stoll, H.; Preuss, H. Energy-Adjusted Ab Initio Pseudopotentials for the Rare Earth Elements. *J. Chem. Phys.* **1989**, *90* (3), 1730−1734.
(56) Cao, X.; Dolg, M.; Stoll, H. Valence Basis Sets for Relativistic Energy-Consistent Small-Core Actinide Pseudopotentials. *J. Chem. Phys.* **2003**, *118* (2), 487−496.
(57) Cao, X.; Dolg, M. Segmented Contraction Scheme for Small-Core Actinide Pseudopotential Basis Sets. *J. Mol. Struct.: THEOCHEM* **2004**, *673* (1−3), 203−209.
(58) Küchle, W.; Dolg, M.; Stoll, H.; Preuss, H. Energy-Adjusted Pseudopotentials for the Actinides. Parameter Sets and Test Calculations for Thorium and Thorium Monoxide. *J. Chem. Phys.* **1994**, *100* (10), 7535−7542.
(59) Pantazis, D. A.; Neese, F. All-Electron Scalar Relativistic Basis Sets for the Actinides. *J. Chem. Theory Comput.* **2011**, *7* (3), 677−684.
(60) Pantazis, D. A.; Neese, F. All-Electron Basis Sets for Heavy Elements. *Wiley Interdiscip. Rev. Comput. Mol. Sci.* **2014**, *4* (4), 363−374.
(61) Douglas, M.; Kroll, N. M. Quantum Electrodynamical Corrections to the Fine Structure of Helium. *Ann. Phys. (Amsterdam, Neth.)* **1974**, *82* (1), 89−155.
(62) Hess, B. A. Relativistic Electronic-Structure Calculations Employing a Two-Component No-Pair Formalism with External-Field Projection Operators. *Phys. Rev. A: At., Mol., Opt. Phys.* **1986**, *33* (6), 3742−3748.
(63) Jansen, G.; Hess, B. A. Revision of the Douglas-Kroll Transformation. *Phys. Rev. A: At., Mol., Opt. Phys.* **1989**, *39* (11), 6016−6017.
(64) Glendening, E. D.; Landis, C. R.; Weinhold, F. Erratum: NBO 6.0: Natural Bond Orbital Analysis Program. *J. Comput. Chem.* **2013**, *34* (24), 2134−2134.
(65) Glendening, E. D.; Badenhoop, J. K.; Reed, A. E.; Carpenter, J. E.; Bohmann, A.; Morales, C. M.; Karafiloglou, P.; Landis, C.; Weinhold, F. *NBO 7.0*; Theoretical Chemistry Institute, University of Wisconsin: Madison, WI, 2018.
(66) Keith, T. A. *AIMA11*; TK Gristmill Software: Overland Park, KS, USA, 2019.
(67) Te Velde, G.; Bickelhaupt, F. M.; Baerends, E. J.; Fonseca Guerra, C.; van Gisbergen, S. J. A.; Snijders, J. G.; Ziegler, T. Chemistry with ADF. *J. Comput. Chem.* **2001**, *22* (9), 931−967.
(68) *ADF*; SCM, Theoretical Chemistry, Vrije Universiteit: Amsterdam, The Netherlands, 2017.
(69) Van Lenthe, E.; Baerends, E. J.; Snijders, J. G. Relativistic Regular Two-component Hamiltonians. *J. Chem. Phys.* **1993**, *99* (6), 4597−4610.
(70) Van Lenthe, E.; Baerends, E. J.; Snijders, J. G. Relativistic Total Energy Using Regular Approximations. *J. Chem. Phys.* **1994**, *101* (11), 9783−9792.
(71) Van Lenthe, E.; Baerends, E. J. Optimized Slater-Type Basis Sets for the Elements 1−118. *J. Comput. Chem.* **2003**, *24* (9), 1142−1156.

https://doi.org/10.1021/jacs.1c03236
J. Am. Chem. Soc. 2021, 143, 9813−9824